Emergent spatiotemporal patterning of synthetic Notch signal transduction *in vivo*

Jonathan E. Dawson[1], Abby Bryant[2], Trevor Jordan [2],
Amber Ajamu-Johnson[2], Paul Langridge [2*†], Abdul N. Malmi-Kakkada[1*†]

[1]Department of Physics and Biophysics, Augusta University, Augusta, GA 30912, USA
[2]Department of Biological Sciences, Augusta University, Augusta, GA 30912, USA

07/11/2023

Cell-cell communication through direct contact is essential during multiple fundamental biological processes. Synthetic forms of contacted-mediated cell-cell communication can generate custom gene expression outputs, making them valuable for tissue engineering and regenerative medicine. Mechanisms underlying the spatiotemporal behavior of synthetic signal outputs in growing tissues, necessary to precisely control the output location and timing, are not well understood. Towards this goal, we combine theory and quantitative experiments to study patterns of synthetic Notch (synNotch) activation - a custom synthetic gene circuit that we implement within growing *Drosophila* wing imaginal discs. We show that cell growth, division, output synthesis and degradation are the key

*Corresponding authors:plangridge@augusta.edu, amalmikakkada@augusta.edu
†Senior co-authors

minimal parameters that predict the heterogenous spatiotemporal patterns of synNotch activation in tissues. At long times, synNotch output forms a graded exponential spatial profile that extends several cell diameters from the signal source, indicating a role of cell division in signal propagation. Furthermore, we discover that the shape of the interface between ligand and receptor cells is important in determining the synNotch output. Overall, we elucidate key biophysical principles that underlie complex emergent spatiotemporal patterns of synNotch output in growing tissues.

Introduction

Synthetic biology combines biological and engineering principles to regulate cellular processes and is emerging as an important area of biomedical research. Synthetic means of manipulating interactions between cells to control tissue behavior has enormous potential for biomedical applications since it would allow natural developmental programs governing growth, differentiation or cell death to be deployed at customized times or locations (*1–3*). Such engineered intercellular communication could allow the initiation of natural cellular processes that develop tissue into customizable forms required for tissue engineering or regenerative medicine applications (*4*). At the same time, synthetic approaches offer an opportunity to learn more about the principles governing the development of native tissues (*5*). This is because synthetic programs can mimic native ones (*6*) that use precise positional signals for the spatial patterning of cellular differentiation and growth (*7–9*). However, deploying synthetic signals *in vivo* to produce a desired response remains a major challenge, and little is known about the capacity of current technologies to achieve this goal.

The challenge is to design synthetic signaling systems to create an output at precise times and locations, such that cells gain positional information and regulate cell-fate decisions (*10–12*). Quantitative experimental studies combined with mathematical and computational modeling have shown that morphogen diffusion creates concentration gradients that can regulate cell growth and cell identity in tissues (*13, 14*). Recent studies on the spatiotemporal patterning of output in contact-mediated signaling circuits have mainly focused (i) on reconstructing the dynamics of intracellular signaling at the single and multicellular scales (*15, 16*), and (ii) at the confluent tissue scale, on the dependence of cell contacts, shape and size, on signal output (*17, 18*). These approaches pertain to cell

contact-mediated signaling in fixed domains rather than within rapidly proliferating tissues relevant during both embryogenesis and tumorigenesis. Knowing how tissue growth with the consequent increase in cell number and changes in the spatial arrangement of signal-sending and receiving cells may alter such engineered responses is an important next step. To address this challenge, here we develop a synthetic cell-cell signaling tool kit for use in the developing wing imaginal disc of *Drosophila*, together with a minimal mathematical model which sheds light on crucial *in vivo* synthetic signaling characteristics in growing tissues. We verify our model by comparing with *in vivo* synNotch output quantifications, and discover that contact-mediated activation of synNotch coupled with cell division in growing tissues set up an emergent graded spatial output profile. Rather than being restricted only to the synNotch cells at the interface, we find that the output extends into the clone, depending on the rates of output biosynthesis, degradation and cell division. Additionally, our approach allows us to glean complex biologically relevant multi-scale parameters such as signal synthesis and degradation rates which are difficult to measure experimentally.

Results

A synNotch circuit in proliferating *Drosophila* epithelia

We produced a synthetic contact-mediated signaling system based on the Notch receptor, an important and pervasive signaling system in the development of all animals (see Materials and Methods Section 1) (*19, 20*). The Notch receptor and its ligands, such as the Drosophila ligand Delta, are single-pass transmembrane proteins. Delta, presented on the cell surface, binds to the ectodomain of Notch on neighboring cells and this physical interaction activates the receptor by inducing proteolytic cleavage of Notch. This results in the intracellular domain moving to the nucleus to act as a transcriptional activator of

Notch target genes, such as Cut (as described in detail, Fig 1(A)). synNotch uses the same activation mechanism but uses heterologous functional domains (Fig 1(B)). This provides a simplified juxtacrine signaling system for analysis *in vivo* since the signal inputs and outputs can be customized and operate orthogonally to endogenous signal systems that govern normal tissue growth. Previously, forms of Delta where the extracellular domain are replaced with Follicle Stimulating Hormone (FSH) were shown to activate chimeras of Notch with the FSH receptor (FSHR) binding regions (*21*). To produce a functional synNotch receptor, we modified FSHR-Notch by introducing heterologous cleavage and transcription factor domains, to produce FSHR-synNotch (described in detail Fig 1(B)). We deploy FSHR-synNotch in the Drosophila wing imaginal disc, an epithelial tissue within which patterning and growth are exceptionally well understood (*22–24*) and with established techniques for controlling and monitoring signaling events (*25, 26*). During development, the wing disc grows from around 5-40 cells a few hours after oviposition to around 40,000 cells at the late third instar where signaling events can be conveniently measured (*27*). As in previous work with FSHR-Notch, the proteins were overexpressed with the UAS/Gal4 system in the Drosophila wing disc in signal sending or signal receiving populations using Mosaic Analysis by Promoter Swap (MAPS). The genetics is described in detail in the methods and in Ref. (*28*), but briefly, the technique subdivides the third instar wing disc into clonal populations of cells expressing FSH-Delta (referred to as 'ligand clones') and cells expressing FSHR-synNotch (referred to as 'synNotch clones'). Expressing these components does not change Cut expression nor the development of the wing (see Supplementary Information (SI) Section 1 and Fig.S1), indicating that FSHR-synNotch operates orthogonally to native Notch.

At the interface of ligand and synNotch clones in the third instar wing disc (referred to here simpy as 'wing'), a surface GFP output is expressed within synNotch cells much

as we anticipated (Fig 1(B)). However, the GFP intensity in the synNotch cells along the interface is not uniform (cells with different intensities are marked with arrows in Fig 1(B)). In some instances, the GFP output is detected in synNotch clones not in contact with the ligand or FSH-Delta clone (arrowheads in Fig. 1(B)). This suggests that in proliferating epithelial tissues the synNotch response is variable and not restricted to those synNotch cells in direct contact with ligand cells as might be expected with a juxtacrine signal. To better understand the heterogeneity in output patterns, we turn to computational modeling as we discuss further below.

Computational biophysical model for synNotch activation predicts that output heterogeneity depends on clonal shape

Changes in cell size, geometry, and cell mechanical properties may impact synNotch output and more generally be important in determining how tissues are patterned through cell-cell contact based signaling during morphogenesis (*29, 30*). Together with tissue growth, the final tissue shape emerges due to a combination of cell division, death, shape changes and position rearrangements (*31, 32*). In this context, complex spatiotemporal synthetic signaling output patterns may emerge. To successfully control and predict the time, location, and extent of synNotch outputs within growing tissues, we surmise that it will be necessary to understand how proliferation dependent changes in the shape of ligand-synNotch interface influence the output (Fig. 1(C i,ii)). To address this, we develop a vertex-based mathematical model of spatiotemporal synNotch activation in proliferating tissues. Cells are represented as two-dimensional polygons (*33, 34*), with chemomechanical coupling between vertex and intracellular synNotch output, including cell growth, and division (Fig. 1(D) and see Materials and Methods Sections 2-4 for details of the model). Our model accounts for cell mechanical properties such as cell volume incompressibility,

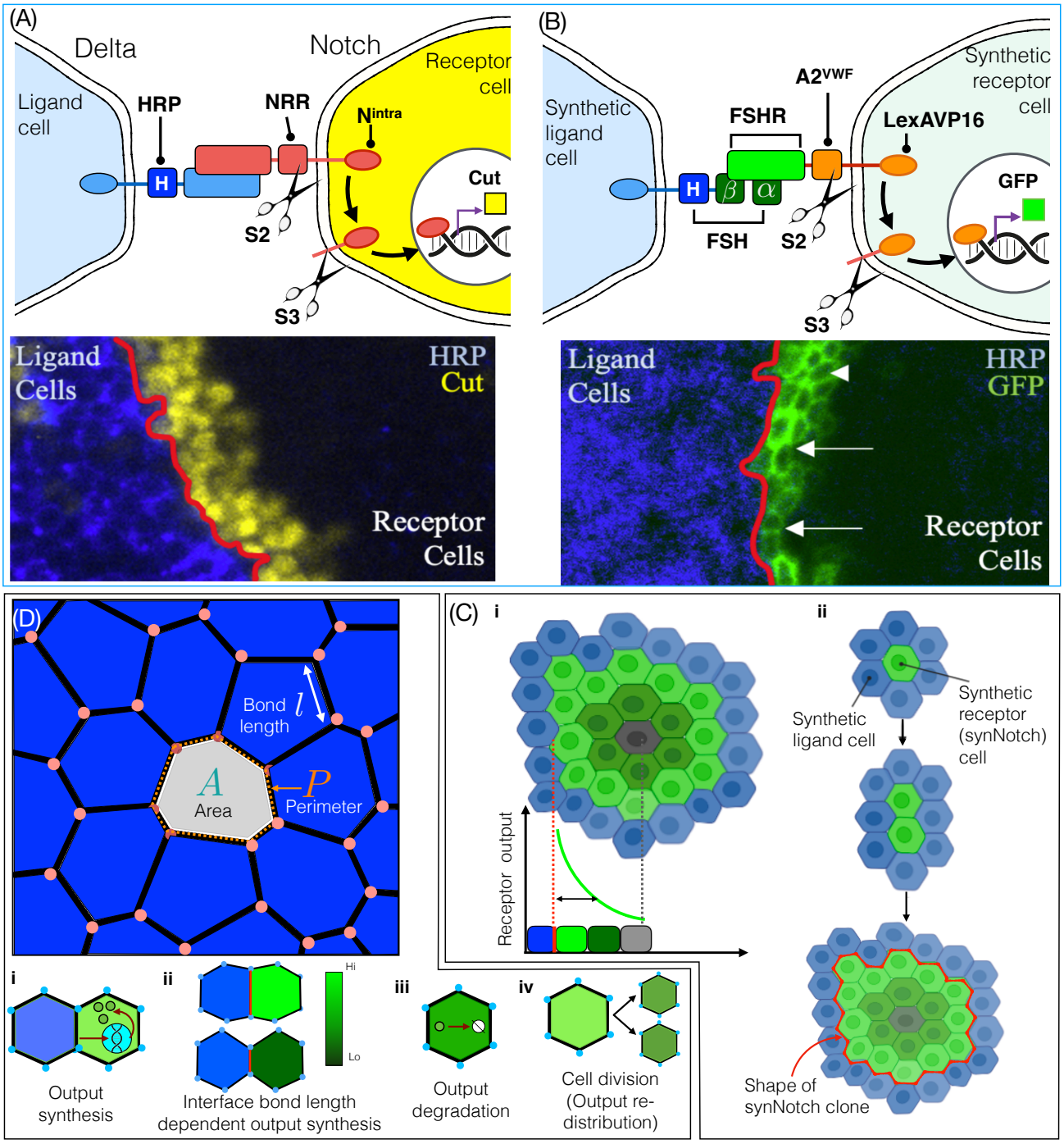

Figure 1: Caption on next page

Figure 1: ***In vivo* synNotch activation and its *in silico* computational model implementation in proliferating wing epithelial cells. (A)** (A) Top: Schematic of native Drosophila Delta binding to Notch on the surface of a signal-receiving receptor cell, which induces the S2 cleavage of the Negative Regulatory Region (NRR). After S2 cleavage, the intramembrane S3 cleavage allows nuclear access of the intracellular domain (N^{intra}), and activation of target genes such as *Cut*. Bottom: Confocal image of ectopic *Cut* expression (native output) in the nuclei of wing cells overexpressing Notch (receptor) adjacent to cells overexpressing Delta (ligand). (B) Top: Schematic of FSHR-synNotch activation. The synNotch activation mechanism is the same as native Notch, although the following components of the receptor and ligand differ. The Delta extracellular domain was replaced with the β-subunit of follicle stimulating hormone (FSH), and FSHα was co-expressed to reconstitute the composite FSH ligand (FSH); the ligand binding region of the Notch ectodomain was replaced by the FSH receptor ectodomain (FSHR); the NRR was replaced with the A2 force sensitive domain; and the intracellular domain was replaced with the lexA-VP16 transcription factor. S2/S3 cleavage and movement of the intracellular domain to the nucleus proceeds as for native Notch, but in this case the target gene activated is the lexO CD2r-GFP transgene. Bottom: Confocal image of lexO CD2r-GFP (output) at the surface of wing cells overexpressing FSHR-synNotch (synNotch receptor) that are adjacent to cells overexpressing FSH-Delta (synthetic ligand), although the intensity of GFP varies (arrows) and extends several cell diameters from the clone interface (arrowheads). **(C)** In this work we focus on (i) spatial, and, (ii) time-dependent variations in synNotch output patterns in a growing tissue, such as during *in vivo* development of a wing. **(D)** Schematic of the two-dimensional (2D) computational vertex model for synNotch induced gene expression. Cells are represented by polygons (composed of vertices shown as colored dots) with a preferred area A_0 and preferred perimeter P_0. The cell shape is characterized by an energy function that describes the balance between cell area compressibility and cell perimeter contractility (see Section Materials and Methods Section 2 for further details on the model). Our model takes into account biological processes governed by different timescales, (i) cell-cell contact length dependent GFP output synthesis rate, (ii) the output synthesis rate dependent on the length of the shared cell bond between ligand and receptor synNotch cell, (iii) GFP degradation rate and (iv) cell division rate. Cell division redistributes the total GFP of the parent cell equally between the two resulting daughter cells (iv).

active contractility due to actomyosin cortex, and cell-cell adhesion (*33*) (see Materials and Methods Section 2). The *in silico* tissue (Fig. 1(D)) consists of two cell types – synNotch cells that initially are uncolored (Fig. 1(D), gray), but can produce GFP output (Fig. 1(D-i), green), and ligand-presenting cells (Fig. 1(D), blue) that can signal to adjacent synNotch cells. The strength of the GFP output in synNotch cells is represented by a green color scale, with black color representing no GFP output and bright green color representing high GFP output (Fig. 1(D-ii)). We hypothesize that the rate of change of GFP output (G_α [arbitrary units]) with time (t) is governed by the dynamic equation,

$$\frac{dG_\alpha(t)}{dt} = S\sum_\beta \frac{l_{\alpha\beta}(1-\delta_{T(\alpha),T(\beta)})}{P_\alpha(t)} - DG_\alpha, \tag{1}$$

where, $l_{\alpha\beta}$ is the cell-cell contact junction length, and P_α is the perimeter of the synNotch cell $\alpha = 1, 2, 3...N$, with N being the total number of synNotch cells. The summation is over all the cells β in contact with a cell α. GFP is synthesized only in those synNotch receptor cells that are in contact with the synthetic ligand-expressing cells as enforced by the delta function term (see Materials and Methods Section 4 for further details). The first term on the right-hand side of Eq. (1) describes GFP output synthesis at the rate S $[h^{-1}]$ (Fig. 1(D-i), h^{-1} denotes 1/hour) and increases with larger contact lengths between synNotch and ligand cells (Fig. 1(D-ii)) (*17*). Hence, the level of GFP output in a synNotch cell, at the interface of the ligand-synNotch clone, is proportional to the instantaneous length of the synNotch cell bond shared directly between the synNotch and the ligand cell. The cell-cell contact junction length can vary as a function of time due to growth-driven cell shape changes and cell division events, capturing intrinsic cellular level processes during wing disc growth. Another important parameter is the degradation of the GFP output in a synNotch cell at the rate D $[h^{-1}]$ (Fig. 1(D-iii)). As cell growth and division are important parameters in our study, we implement specific rules for such cell behaviors. A cell divides along its short axis when its area doubles, resulting in tissue growth over time (see Materials and Methods Section 3 for details). Upon division, the total amount of GFP output in a parent cell is distributed equally between the two resulting daughter cells (Fig. 1(D-iv)). The simulation initial conditions and the relevant parameter values are listed in Table (1). Having briefly introduced the model, we now describe the results.

Due to repeated cycles of cell growth and division, the clone size expands over time, giving rise to increasing numbers of synNotch receptor/ligand cells, Fig. 2(A) and SI Movies 1-3. Snapshots of an expanding synNotch clone are shown at 3 distinct time points as highlighted with yellow bars in the inset. We predict that the distribution of synNotch

output in expanding *in silico* tissues exhibits complex heterogeneous spatial patterns. Initially, there is one synNotch cell that strongly expresses GFP as it is surrounded on all sides by ligand cells (see the first yellow bar in Fig. 2(A) inset). After $\sim 50h$-$80h$ of tissue growth, GFP expression among cells shows marked heterogeneity with higher output at the border cells compared to those in the clone interior. This spatial pattern is seen in FSHR-synNotch clones following 24, 48 and 72 h of proliferation in Fig. 2 (B-D), showing confocal images of the Drosophila wing with ligand cells (blue) and synNotch cells expressing GFP as output. At earlier time points, all synNotch cells are directly in contact with ligand cells and express GFP (Fig. 2(B-C)). However, at $t = 72h$, the spatial output pattern is heterogenous with GFP expression pronounced at the boundary while cells in the clone interior express little/no GFP (Fig. 2(D)), in agreement with our *in silico* predictions.

We reasoned that heterogeneous synNotch output patterns are likely because cell growth and division lead to highly dynamic contact interface lengths between synNotch and ligand cells, giving rise to new interfaces and displacing cells away from the interface. Hence, cell division events and changes in cell-cell contact lengths together causes variations in the synNotch clone shape, possibly accounting for the heterogeneous spatial synNotch output patterns that we observe. By quantifying the time-dependent clone shape change, we sought to ascertain whether the heterogeneity in the signal output pattern is influenced by the clone shape. As the clone expands, together with the total GFP output (Fig. 2(E)) both its overall area (A) and its boundary perimeter (P) increase. We measure the clone circularity, $4\pi A/P^2$, a shape parameter whose value is 1 for a circle and approaches 0 for highly distorted shapes, see the inset of Fig. 2(F). The clone shape changes markedly as it expands, evolving from a fairly circular shape to a highly distorted shape characterized by a rough interface (Fig. 2(F)). Notably, our model allows us to link

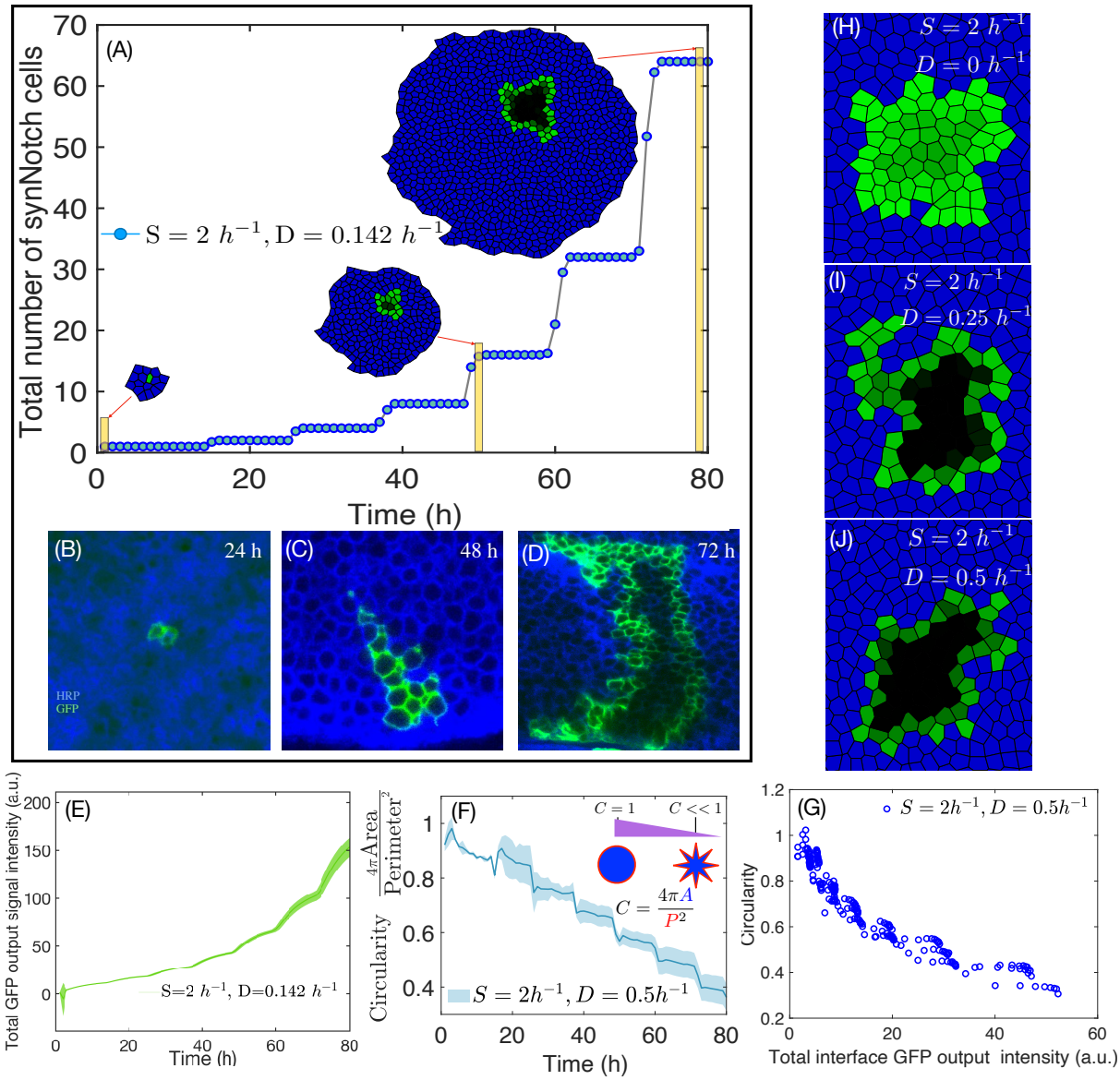

Figure 2: Caption on next page.

Figure 2: **Emergent spatial synNotch output pattern in growing tissues due to clonal shape variations. (A)** Time-dependent behavior of the total number of synNotch cells in a growing tissue *in silico*. The initial state of the tissue consists of ~ 15 ligand cells (blue colored) and one initiated Notch cell (colored in green). As the tissue expands, due to multiple cell division events, (*in silico* tissue shown at three different times for fixed values of S and D), the number of synNotch cells grows over time to about 60 cells at the end of 80 h. **(B-D)** Confocal images of distinct Drosophila wing imaginal discs at 24, 48 and 72 h after clonal generation of populations of FSHR-synNotch (uncolored and green) and FSH-Delta (blue) expressing cells by mitotic recombination. At 24 h after recombination small clones of only a few cells are visible and all express lexO cd2r-GFP. Such clones appear larger at 48 h with all cells expressing GFP. By 72 h the FSHR-synNotch clone is large enough that significant number of cells are far from FSH-Delta cells and do not show GFP fluorescence. Qualitatively the images appear similar to modelled clones at similar time points, as shown in (A). **(E)** The total amount of output GFP expression in the whole synNotch clone as a function of time for fixed value of output synthesis and degradation. The data is averaged over 3 simulation runs. The shaded area represents the standard deviation here and henceforth. **(F)** Time-dependent behavior of the shape of the synNotch clone as quantified by the circularity parameter. A perfect circle has a circularity of 1 and a highly distorted or elongated shape has a circularity approaching 0 (see Inset). **(G)** Total GFP output intensity in the interface synNotch cells is higher for lower values of synNotch clone circularity. This indicates strong influence of the synNotch clone shape on the GFP output. **(H-J)** Pattern of GFP signal intensity (synNotch output) in synNotch cell populations after $t = 80h$ for fixed synthesis rate and varying signal output decay rates as shown in the legends.

clone shape to synNotch output. Using the mathematical model, Eq.(1), we predict that the total GFP output is inversely proportional to the clone circularity (see Materials and Methods Section 5). This implies that a clone that is circular in shape will have lower GFP output while a highly irregular-shaped clone would have a higher GFP output. To test this key prediction, we focus our analysis on cells at the interface between ligand and synNotch cells as the shape of the clone is determined by these cells. The GFP output in the synNotch clone cells at the interface depends strongly on the clone shape (Fig. 2(G)), in agreement with our predictions. The output is low when the clone shape is highly circular, while high output is obtained when the clone shape is highly irregular. Therefore, as the GFP output is inversely proportional to the clone circularity we ascertain that clone shape is important in determining cell-cell contact-based signal output patterns.

To further understand the role of clone shape in determining the synNotch output, we look into the spatial distribution of GFP output within the synNotch clone. We observe

generally that the border synNotch cells adjacent to ligand cells have high intensity of GFP output (bright green), which gradually weaken (light green to gray) towards the center of the clone (Fig. 2(H-I)). The lower intensity of the output at the clone center could be due to the absence of GFP production in synNotch cells that lose contact with the ligand cells. While there is an absence of GFP production, degradation of GFP continues to occur which we anticipate will cause the GFP intensity to be weaker in the interior synNotch cells. If this is indeed the mechanism at play, we expect the GFP intensity within the synNotch clones to be strongly dependent on the degradation parameter D. For small D, representing a slower output decay rate, large variations in GFP expression across the synNotch clone are not seen (see Fig. 2(H)). Notably, as shown in Fig. 2(H), synNotch cells not directly at the clone border also express significant levels of GFP. At the intermediate value of $D = 0.25h^{-1}$ in Fig. 2(I), a "donut"-like pattern emerges with little to no GFP (gray) in cells at the clone interior while cells at the periphery express high GFP levels. At even higher values of the output decay rate (D), the "donut"-like pattern is preserved but GFP in the peripheral cells is also lower, leading to more marked heterogeneity in GFP levels amongst cells (see Fig. 2(J)). Taken together, our results suggest that (i) the total GFP output in the synNotch clone is determined not only by the total number of synNotch cells but also by the clone shape, (ii) GFP output pattern within the clone is determined by the intracellular GFP output degradation rate. Of note, some synNotch cells show significant output despite being not in direct contact with ligand cells. This unexpected observation leads to a spatial propagation of signal output, which we investigate further below.

Output signal propagation into the clone is characterized by exponential decay and is a function of the output degradation rate

The establishment of a spatial morphogen gradient with variation in the concentration of transcription factors or signaling molecules across a field of cells is the most widely accepted framework for pattern formation in developing organisms (*35, 36*). In this framework, cells determine their spatial location from local measurements of morphogen concentration. While morphogens set up a spatial gradient across a tissue by diffusion, whether such gradients can be produced by juxtacrine signaling is unclear. We turned to our *in silico* model to address the question of whether synNotch based intercellular signaling can establish a spatial gradient in synNotch output and which model parameters are important in this regard.

Our observations point to output degradation rate as an important parameter in controlling the spatial gradient of GFP output across the synNotch cell clone. As such, we fixed the rates of synNotch GFP output synthesis (S) at $2h^{-1}$ and vary D from $0 - 0.5h^{-1}$. This includes the physiologically relevant value of $D \sim 0.142h^{-1}$ reported in the literature (*37, 38*). To quantify the gradient of GFP output across the clone, we sought to reproducibly generate GFP output versus distance along the spatial region traversing the boundary and interior of the synNotch clone. The spatial output profile is characterized by higher GFP output in cells at the clone boundary, and a gradient with lower GFP in the clone interior (see Fig. 3(B)). With increasing D, the GFP output decays more steeply as one moves from the border to the center of the synNotch clone, based on the normalized GFP output profile in Fig. 3(C). The GFP intensity normalized to that of the first synNotch cell in the horizontal strip (Fig. 3(C)) is well described by an exponentially decaying function of the form e^{-i/i^*}, where i is the cell index. $i = 1$ is the index of the first synNotch cell in the horizontal strip, and i^* is the characteristic number of

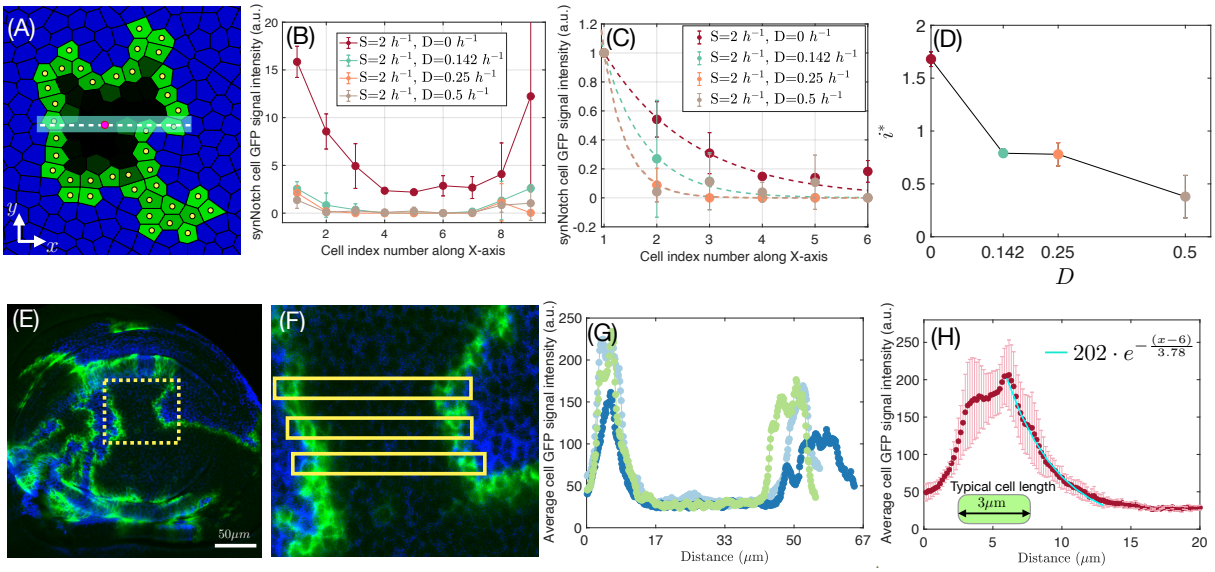

Figure 3: **synNotch output decays exponentially away from the clonal interface in an output degradation rate-dependent manner (A)** The spatial profile of synNotch output (i.e. GFP signal intensity), *in silico*, across the receptor cell clone (see white dashed line) at late times, $t = 80h$. We first identify synNotch cells located within a narrow horizontal band that passes through the clone center of mass, i.e., $|y_\alpha - y_{CM}| < 2\ \mu m$, where y_α is y coordinate of a synNotch cell α and y_{CM} is the y component of the center of mass (R_{CM}) of the synNotch clone (see pink dot marking the center and dashed line marking the horizontal strip). $\vec{R}_{CM}$ is defined as $\vec{R}_{CM} = 1/N \sum_\alpha^N \vec{r}_\alpha$, where N is the total number of synNotch cells and $\vec{r}_\alpha$ is the coordinate of a synNotch cell α. **(B)** Simulation results for the GFP signal intensity along the $x-$ axis across the receptor cell clone for fixed output synthesis rate and varying output degradation rate D (see figure legend). Each data point is the mean of three independent simulation runs. Error bars show the standard deviation here and henceforth. **(C)** GFP signal intensity, shown in (B), rescaled by the GFP signal intensity of the first synNotch cell from the left. Rescaled data is fit by an exponentially decaying function (dashed lines) of the form e^{-x/i^*}. **(D)** The value of i^*, obtained from the fits, as a function of D. $i^* = 1.69 \pm 0.074$ for the red curve, 0.79 ± 0.04 for the green curve, 0.78 ± 0.1 for the orange curve, and 0.38 ± 0.2 for the brown curve corresponding to the decay rates in the inset of panel (C). **(E)** Confocal image of lexO cd2r-GFP (green) at the surface of Drosophila wing cells overexpressing FSHR-synNotch that are adjacent to FSH-Delta cells (blue). **(F)** Spatial profile of GFP output was quantified along three different horizontal sections across the clone as shown by the three yellow boxes. GFP intensity is averaged over the box width. **(G)** Spatial GFP output profile at three different locations across the synNotch clone. The origin is the left end of the yellow boxes shown in (F). The two peaks correspond to the interface region between ligand and synNotch receptor cells. **(H)** Average of the three spatial profiles of GFP output near the interface. Magenta-filled circles represent the mean, and the error bars show the standard deviation. The average data is fit by an exponential function of the form Ae^{-x/i^*} (turquoise colored line). $i^* = 3.78\ \mu$m. The average diameter of a synNotch cell is shown in the inset equalling 3μm.

cells from the border over which the GFP level decays exponentially. This analysis allowed us to quantify the number of synNotch cells, starting from the border synNotch cell located

at the ligand-receptor interface, beyond which the strength of the GFP signal output drops significantly by a factor of $1/e$, Fig. 3(D). For no GFP degradation $(D = 0), i^* \sim 2$, suggesting that a drop of $\sim 36\%$ in output intensity is observed beyond 2 cells in the interior of the clone. For $D = 0.5h^{-1}$, $i^* \sim 0.5$, indicating that output intensity decays substantially within one cell layer from the boundary between receptor and ligand expressing cells (see Fig. 3(D)). This allows us to predict the propagation of the GFP output into the synNotch clone in terms of the characteristic number of cell diameters. Our results imply that output degradation rate is an important parameter in determining the extent of output propagation, and that quantifying the spatial output decay by fitting to an exponential function would enable us to deduce the signal output decay rates *in vivo*. Conversely, by fixing the synNotch output degradation rate we can quantify the synthesis rate on the basis of the output spatial profile. As output synthesis rate is a complex multi-scale parameter depending on molecular scale cell events such as the translocation of the synthetic transcriptional activator to the nucleus in addition to cell-cell junction properties, this is a non-trivial prediction which we anticipate will be very useful for improving the predictability of synthetic gene circuit outputs *in vivo*.

Next, we compared our model predictions above with FSHR-synNotch activation *in vivo*, and quantified the fluorescence intensity of the GFP output in synNotch clones adjacent to ligand clones. We measure the GFP output intensity at three different locations in the tissue along a transverse strip across the synNotch cell clone, Fig. 3(E-F), showing a clear peak at the boundary and valley towards the center of the synNotch receptor cell clone, similar to the results obtained from our computational model, compare Figs. 3 (B) and (G). We took the average of GFP intensity profile across the three transverse sections of this clone and fit it to an exponentially decaying function, Fig. 3(H). The fit revealed that the spatial gradient of GFP, from the boundary towards the center of the synNotch

clone, is characterized by a distance scale that corresponds to ~ 1.5 cell diameters. This result is significant, as naively we would expect the response to be strictly confined to those cells in the clone that are directly in contact with the signal-sending ligand cells. Instead, we find a spatially graded signal output, with its maximum at the location of the ligand-synNotch interface and gradually decaying towards the center of the clone. Our analysis further shows that on average the signal propagates a distance which is more than one cell diameter from the perimeter into the receptor clone.

Propagation of synNotch output *in vivo* extends as far as 4 cell diameters from the clonal interface

Our model predicts that synNotch activation in growing tissues form a spatial output gradient which may extend several cell diameters into the clone. To investigate this further, we analyzed *in vivo* examples of signaling interfaces where we clearly detect GFP output beyond the ligand/synNotch interface, and quantified the FSHR-synNotch activation profiles as a function of distance from the interface. To appropriately mark the position of the clonal interface, we use the intensity of anti-HRP antibody staining (Fig. 4(A1-E1)) against the HRP tag of the FSH-Delta ligand. Such HRP staining effectively marks the ligand cell populations and hence the interface between receptor and ligand cells (see yellow line in Fig. 4(A1)). Similarly, the GFP output intensity is obtained as shown in Fig. 4(A2-E2). The expression profiles of both HRP staining (red) and GFP (green) along a horizontal line in the region of interest traversing both ligand cells and synNotch cells are shown in Fig. 4(A3-E3). We defined the clonal interface as the location in the fluorescence intensity profile at which expression levels of HRP staining dropped to 45% from its maximum value (see red dashed lines in Fig. 4(A3-E3)).

To identify the decay length of the GFP output in the clone, we fit an exponentially

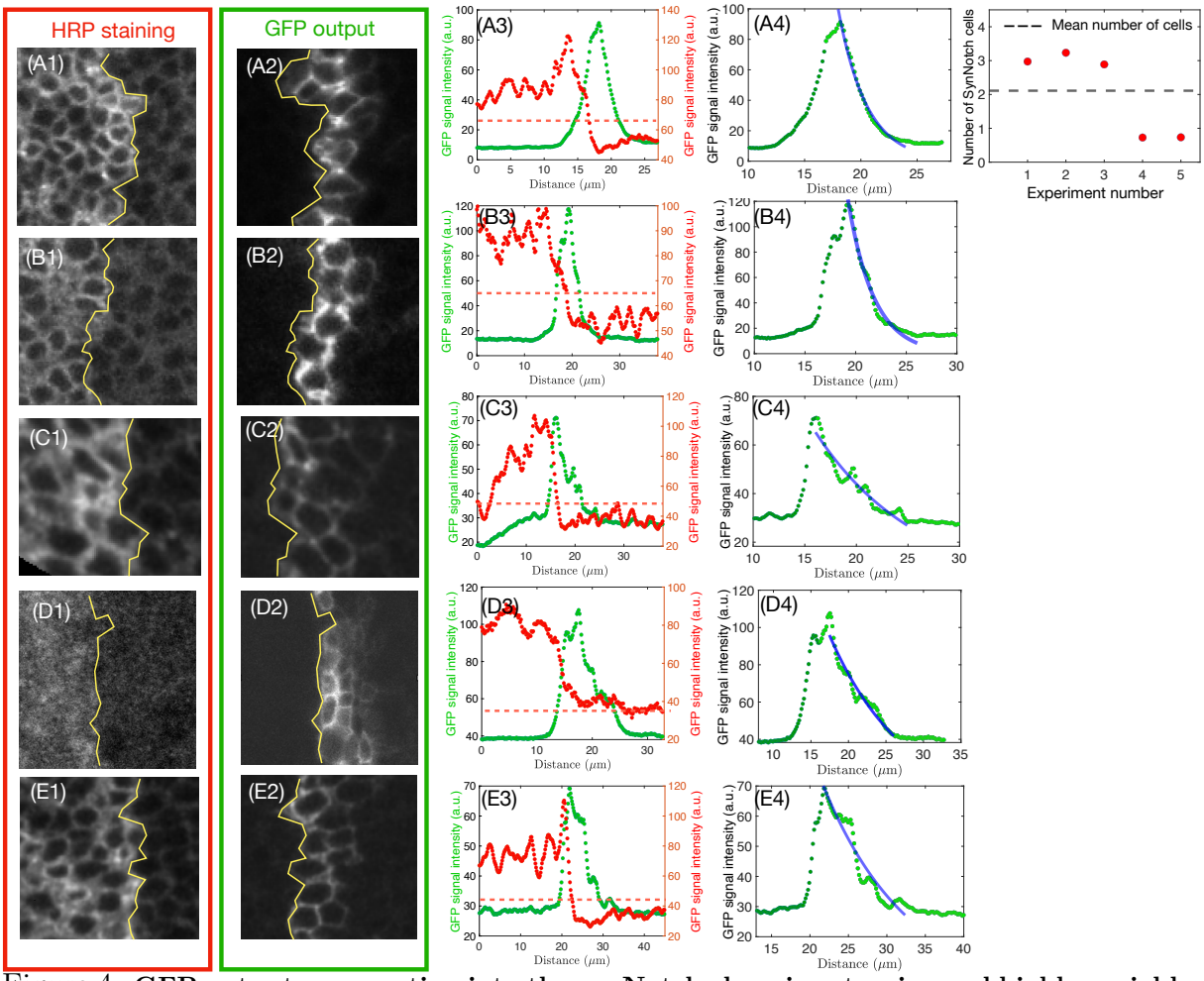

Figure 4: **GFP output propagation into the synNotch clone is extensive and highly variable. (A1-E1)** HRP staining in the *Drosophila* wing disc marks synthetic ligand-expressing cells. Five distinct *in vivo* experiments are shown. **(A2-E2)** GFP output expression in the synNotch cells across from the ligand expressing cells are shown. The boundary between the receptor and ligand expressing cells, as determined by the ligand expression, is marked by the yellow line in panels. **(A3-E3)** In each of the experimental images, HRP staining (red dots) and GFP fluorescence intensities (green dots) were quantified along a straight horizontal line passing through the interface between synNotch and ligand-expressing cells. The resulting fluorescence intensity profiles of the two signals along the length of the line are shown. We identified the interface between the ligand and synNotch receptor cells as the distance where the fluorescence intensity of the HRP signal dropped to 45% of the maximum (shown by dashed red lines). The intensity of the GFP signal output at this location is labeled G_{max}. **(A4-E4)**The exponential functional fit $G_{max}e^{-x/x^*}$ (solid blue curve) to the intensity profile of the GFP signal output within the spatial range starting from the location of G_{max} to the point where the output exhibits a plateau. Across multiple experiments, the output spatial profile is characterized by an exponential form implying the presence of a characteristic spatial scale. **(F)** Quantification, in each experiment, of the number of cells from the clonal interface across which the signal output propagates. We extract the number of cells from the interface and into the clone across which the GFP intensity drops by the factor $1/e$. We use the experimental scale wherein approximately $3\mu m$ corresponds to one cell diameter. The dashed line corresponds to the mean indicating spatial output propagation over 2 cell diameters.

decaying function (as in Fig. 3(H)) to the measured GFP intensity from the interface to the location where GFP intensity profile plateaued at low-intensity values (Fig. 4(A4-E4)). From the individual fits to the experimental data, each of which corresponds to a separate *in vivo* experiment, we obtained the characteristic decay length of the GFP output into the clone (see blue lines in Fig. 4(A4-E4)). Interestingly, the extent of propagation varies greatly with clear examples (in 3 out of 5 experiments) of output signal propagation as far as 3-4 cell diameters away from the clonal interface. In cases where there is a propagation of output beyond the single cell layer at the interface, on average it extends 2 cell diameters into the receptor clone (Fig. 4(F)). Overall our *in vivo* analysis shows that the GFP output can be detected multiple cell diameters away from the ligand-receptor cell boundary and into the clone. Our computational successfully predicted the propagation of the synNotch output, indicating that the division-driven displacement of cells away from the interface may account for this phenomenon.

Output response in synNotch cells at the clonal interface is characterized by strong fluctuations and is highly spatially uncorrelated

Earlier studies have shown that Notch activation depends upon the contact length between the signal-sending and signal-receiving cells (*17*). By incorporating this property of signal activation in our synNotch model, we observed that output response can be highly heterogeneous. Moreover, given that the clone circularity undergoes significant changes as the tissue expands due to cell growth and division, we anticipate that there will be large variations in the contact length between synNotch and ligand cells along the clone boundary. This could account for highly heterogenous synNotch output at the interface (as in Fig. 2(H-J)). First, we sought to quantify the output heterogeneity along the cells at the clone interface in direct contact with ligand clones (see Fig.5(A) *in silico*). In order to

consistently quantify the GFP output, we assign angular positions θ_i to border synNotch cells i, where $\theta_i = \tan^{-1}(\frac{\mathrm{y_i - y_{cm}}}{\mathrm{x_i - x_{cm}}})$ is defined with respect to the $x-$ axis and (x_{cm}, y_{cm}) are the center of mass coordinates of the synNotch clone, marked with pink dot in Fig. 5(A). Individual synNotch cells, sorted according to their angular positions, display large fluctuations in the GFP intensity. The amplitude of the fluctuations depends on the GFP degradation rate D, although at all levels of D, the fluctuations persisted (Fig. 5(B)). Since the intracellular GFP synthesis in the model is dependent on the junction length between ligand and synNotch cells, $l_{\alpha\beta}$, stochasticity in cell growth and the orientation of cell division axes can give rise to irregular interface contact lengths, accounting for the fluctuations in the GFP levels we observe.

We quantify the heterogeneity in the synNotch output along border cells using the angular correlation of GFP intensity fluctuations,

$$C(\theta_k) = \Sigma_{i,j}\delta(\theta_k - (\theta_i - \theta_j))[(I(\theta_i) - \langle I\rangle)(I(\theta_j) - \langle I\rangle)], \tag{2}$$

where $I(\theta_i)$ is the GFP intensity in cell i whose angular position is θ_i and $i, j = 1...N_b$ are the indices for the total number of boundary cells (N_b). $\delta(z) = 1$ if $z = 0$, and 0 otherwise. $\langle I\rangle$ is the mean GFP intensity over all the cells along the boundary. The autocorrelation function defined in Eq. (2) measures the correlation between signal intensities in individual cells along the border. The decay in the correlation function is an important measure of how similar GFP output levels are between cells with quicker decay indicating low correlation and slower decay denoting strong correlation. We compute $C(\theta_k)$ for both fixed rate of GFP synthesis $S = 2h^{-1}$ with varying GFP degradation rates D (Fig. 5(C)) as well as fixed rate of $D = 0h^{-1}$ with varying S (Fig. 5(D)). In both cases, the correlation of GFP intensity fluctuations along the border synNotch cells exhibits fast decay with respect to the change in angular positions (θ_k). This implies that the cell-to-cell variations

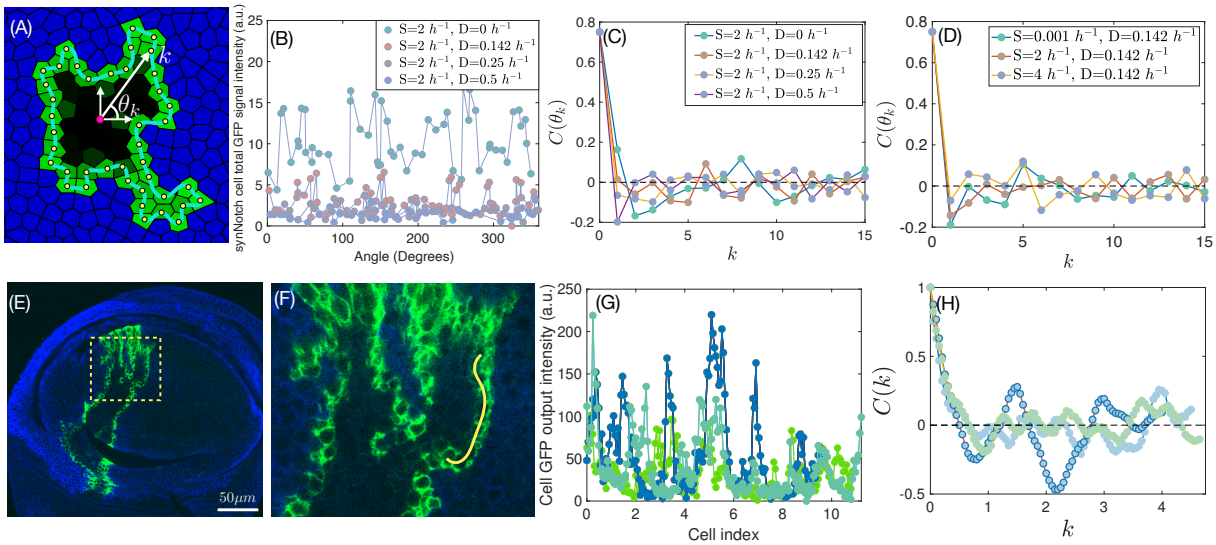

Figure 5: **Output along the boundary of synNotch cell clone is highly spatially uncorrelated.** **(A)** The spatial profile of GFP output in synNotch receptor cells quantified along the border cells at the synthetic receptor-ligand expressing cell interface at $t = 80h$. The angular position of a border synNotch cell k is obtained from coordinates of the cell center (x_k, y_k) and the center of mass of the synNotch cell clone (x_{CM}, y_{CM}) as, $\theta_k = \tan^{-1}(\frac{y_k - y_{CM}}{x_k - x_{CM}})$. **(B)** Total GFP signal intensity in the border synNotch cells as function of the cell angular position θ_k for a fixed value of $S = 2h^{-1}$ and different values of $D = 0h^{-1}, 0.142h^{-1}, 0.25h^{-1}, 0.5h^{-1}$. **(C,D)** Autocorrelation function of the of GFP signal intensity in the border synNotch cells for (C) fixed $S = 2h^{-1}$ and varying D, and for (D) fixed $D = 0.142h^{-1}$ and varying S. Fast decay in the output intensity fluctuation correlation is characteristic of the high variability in the output between synNotch cells at the border. **(E)** Fluorescence microscopy image of *in vivo* FSHR-synNotch activation in the *Drosophila* wing imaginal disc. Green color shows the fluorescence intensity of the GFP output in synNotch cells, and the blue color marks ligand cells. **(F)** Zoom-in image from panel (E) showing the spatial profile of GFP output quantified along the border of synNotch clone (along the yellow line). **(G)** GFP output intensity, rescaled to the typical cell size of $3\mu m$, along the border of the synNotch clone. The three curves represent different boundary segments. **(H)** Autocorrelation analysis of fluctuations in the GFP output intensity along the border of the synNotch clone shows rapid decay to zero. This indicates a very low correlation of GFP output along the cells at the border.

in GFP output at the ligand-synNotch clone border are independent of the rates of both GFP synthesis S and GFP degradation D. Therefore, unlike the output propagation into the clone that is largely dependent upon decay rates, output spatial pattern along the clone boundary shows no dependence on either S or D. This is consistent with the idea that the variability in cell-cell contact length along the border cells could determine the magnitude of the output response. In our model, two main sources of variability in the cell bond length are (i) cell growth and (ii) the random orientation of cell divisions. These

could lead to strong fluctuations in GFP intensity along the border cells.

We tested our model predictions by quantifying the fluorescence intensity of GFP output in synNotch cells along a section of the clone boundary in multiple wing discs, as shown in Fig. 5(E) and the zoom-in image in Fig. 5(F). The GFP intensity profiles obtained were quantitatively similar to the simulations, with large fluctuations in the GFP intensity along the border of the synNotch clone, Fig. 5(G). Note that there is a difference in the GFP quantification between the simulation and *in vivo*. In the simulations, we track GFP output per cell while in the experiments we track GFP output at the cell border. Given that we average over a line of finite thickness in the *in vivo* quantifications, we are able to make a direct comparison with the simulations. By performing the autocorrelation analysis of the experimental data according to Eq. (2), we observe that the GFP output correlation decays rapidly (Fig. 5(H)). $C(k) \sim 0$ within 1 cell neighbor, in agreement with our model predictions. Here, we rescale the distance along the synNotch clone border into cell index (k) based on cell size quantification from *in vivo* images (20 pixels = $3\mu m$ = 1 cell diameter). The excellent agreement in the spatial correlation of the output intensity between simulation predictions and experiments enables us to conclude that variations in cell-cell contact lengths could be the primary contributor to the heterogeneity in the output intensity along the border synNotch cells. We investigate the impact of variations in cell-cell contact length on signal output in further detail below.

Large variations in the cell-cell junction interface length leads to highly heterogeneous synNotch output response

We anticipate that the cell-cell contact interface length is a highly dynamic variable that changes due to cell shape fluctuations together with cell growth and division events. Within growing tissues, individual cell-cell contact length is likely important in determin-

ing both the magnitude and the spatial gradient of the GFP output. As such, we sought to quantify how the variations in the length of an individual synNotch cell's bond at the interface between synNotch and ligand clones influences intracellular GFP output. The entire synNotch clone from one representative *in silico* realization is shown in the left inset of Fig. 6(A) with a zoom-in into the region marked by the dashed line box shown in the main panel. The individual cell-cell contact lengths for 5 cells along the border are marked in different colors. There are marked differences in not only the cell-cell contact lengths but also the number of ligand cells (colored blue) that are in contact with a given synNotch cell (colored green/black). Note that some synNotch cells make contact with a single ligand cell (see Cell #1 and Cell #3 in Fig. 6(A)) while Cell #4 makes contact with 4 distinct ligand cells.

We observe a linear dependence between the cell-cell contact length and GFP output. This is surprising given that the rate of intracellular GFP synthesis S is constant for all the synNotch cells along the border. Nevertheless, high variability in the output emerges due to higher GFP output in the border synNotch cells which have longer contact lengths, Fig. 6(B-D). This can be understood from our model by considering the equation governing the dynamics of GFP signal output in synNotch cells (Eq. (1)). The term representing intracellular GFP synthesis depends not only on S but also on the length of the ligand synNotch interface cell bond, $l_{\alpha\beta}$. We anticipate that in a growing *Drosophila* wing disc, cell growth and cell elongation, resulting in apical surface expansion, and orientation of cell division act collectively to give rise to the observed variation in interface cell bond length. This active cell growth process and the associated cell mechanical properties, therefore, have direct implications on the output spatiotemporal patterns obtained from cell-cell contact-based signaling. As mechanical forces generated by myosin, actin (*39*) together with cell-cell adhesion molecules (*40*) can regulate the cell-cell contact length,

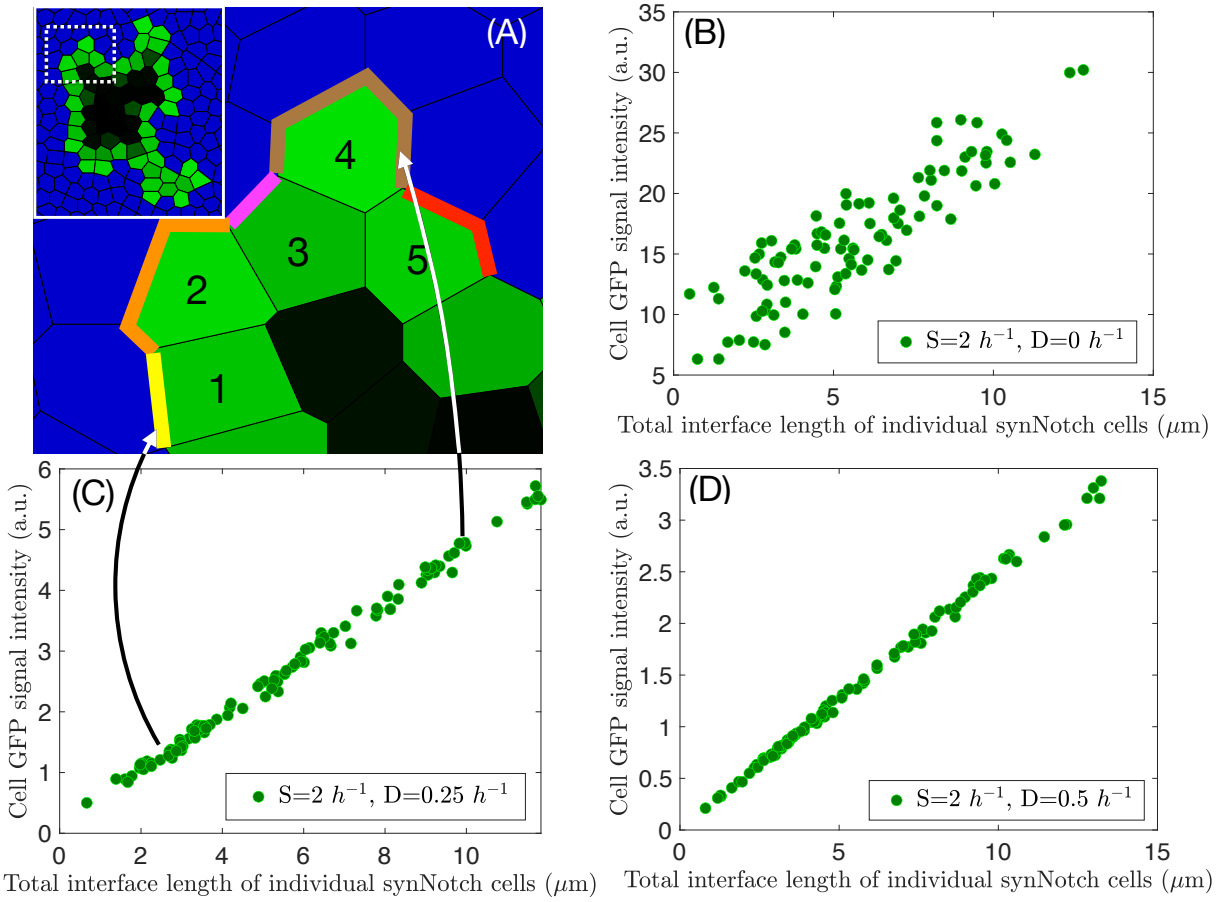

Figure 6: **GFP output varies in proportion to cell-cell contact length between synNotch and ligand cells. (A)** Cell division and cell area growth give rise to different total interface lengths for each border synNotch cell. The entire synNotch clone is visible in the left inset, and the zoom-in view of the highlighted portion of the clone is shown in the main panel. Individual cells are labeled 1 through 5 with their total cell-cell contact length shared with the ligand cells colored. **(B-D)** GFP output intensity in the border synNotch cells versus the total cell-cell contact length between synNotch and ligand cells for a fixed value of $S = 2h^{-1}$ and different values of decay rates (B) $D = 0h^{-1}$,(C) $0.25h^{-1}$ and (D) $0.5h^{-1}$. Examples of small and large values of the individual cell interface length are shown by the arrows. Cell #1 has a smaller contact length with ligand cell (shown in yellow) while Cell #4 has a larger contact length. GFP output shows a linear dependence on the cell-cell contact length, independent of the output synthesis and degradation rates. Output synthesis increases with the junction length of a synNotch cell making contact with a ligand cell.

our results provide insight into how cell mechanical properties could impact signal output in growing clones (*41, 42*). While molecular scale variabilities such as fluctuations in the levels of transcription activity may also impact synNotch output, we show that variation

in cell-cell junction length is an important physical parameter that needs to be considered.

Discussion

In this study, by implementing a combined computational and experimental approach, we elucidate the emergent synNotch output patterns in growing *Drosophila* wing. Despite the complexity underlying synthetic gene expression patterns *in vivo*, our minimal computational model captures key experimentally observed features of the output patterns that emerge following synNotch activation in this tissue. Specifically, our model had the following key parameters, (i) constant cell area growth rate, (ii) output synthesis rate, and (iii) output degradation rate. Although synNotch is activated due to contact with one or more ligand-presenting neighbor cells, we found that synthetic signal output in an expanding clone of synNotch cells self-organizes into a complex pattern determined by synNotch activation coupled to the dynamics of cell growth and division. Specifically, the model leads to (a) self-organized growth of the clone, characterized by continuous change in the clone shape over time, (b) a spatially graded profile of the output across the synNotch clone, characterized by an exponentially decaying function, and, (c) large fluctuations in the output in synNotch cells along the border of the clone, characterized by a very fast decay in the correlation of output fluctuations. We tested our model predictions with *in vivo* experiments and quantitatively assessed similar synNotch output patterns. Consistent with our model predictions, after the experimental period of tissue growth the output formed a spatial gradient of GFP fluorescence across the clone of synNotch cells. Specifically, the GFP intensity profile showed an exponential decay from the border towards the center of the clone, and a variable but significant number of cells had detectable GFP expression several cell diameters away from the clonal interface. Such graded profiles across a tissue are well defined for morphogens, such as decapentaplegic

(Dpp) and Wingless (Wg, a Wnt5 homolog), that diffuse from a population of source cells with their distribution determining the gene expression patterns and cell differentiation to form complex structures such as the wing (*12*). However, as to the question of whether an output gradient can be established in the absence of diffusible signals, our results provide a plausible mechanism for graded juxtacrine signal outputs. When a responding synNotch cell divides, the output is divided equally between the daughter cells making it possible to produce daughter cells that are not in contact with ligand cells, yet continue to exhibit output. If the output persists in the cell for a long enough time, multiple rounds of cell division can produce responding cells several cell diameters into the clone, with the output decaying exponentially as each division halves the output. Propagation of a juxtacrine signal output may well be a general feature of contact-mediated signaling in proliferating tissues like the wing. Our results may have more general implications not directly related to juxtacrine signaling. For instance, the diffusible morphogens Dpp and Wg normally elicit growth and transcriptional responses over 30 cell diameters away from their source, but when tethered or restricted to the surface of producing cells, transcriptional responses can still be detected in cells several cell diameters away from the signal-sending cells (*24*). This may arise due to a similar mechanism as we propose here - due to cell division-driven displacement of cells previously in contact with the tethered signal (*43*).

Alternatively, it is also possible that an output several cell diameters from the clonal interface may be induced by other means. For instance, it has been suggested that basal cell extensions in the epithelium of the fly notum can support long-range Delta/Notch signaling over several cell diameters (*44*) and there is evidence that cell extensions or cytonemes that extend basally across multiple cell lengths in the wing imaginal disc can act as signaling platforms for the morphogen Hedgehog (*45*). In principle, cytonemes could be capable of eliciting a synNotch response far from the interface between the

two cell populations (*46*). Our model does not include such long range contact-based signaling, and restricts signaling to synNotch cells immediately adjacent to the ligand cells. Nevertheless, the model produces patterns where there is a variable but significant number of cells that produce an output away from the ligand interface. Our results therefore suggest that cell proliferation can account for the long range of output without a need to invoke models encompassing specialized signaling modalities away from the clonal interface.

Our *in vivo* experiments show that within synNotch cells the intensity profile of GFP expression in responding synNotch cells along the ligand-receptor interface highly fluctuates with rapidly decaying correlations. Our model suggests that such fluctuations in the intensity of GFP expression arise due to heterogeneity in the interface bond length of the synNotch cells that are in contact with synthetic ligand expressing cells. Our computational model accounts for two prominent sources of cell bond length heterogeneity, (i) stochastic cell area growth, and, (ii) random orientation of cell division. As both these processes are influenced by tension in the cell bond and regulated by subcortical network of cell acto-myosin, our work provides a tool to study and predict the influence of cell bond tension on synNotch driven spatial patterning of the output signal. Depending on the angle of cell division, a responding daughter cell at the clonal interface may be displaced from the interface such that it either completely loses contact with the ligand expressing cells or continues to maintain such contacts. As a result of cell divisions signal-sending/receiving cell contact length may be increased or decreased or contact may be lost altogether, with each scenario bearing an influence on the level of output in the synNotch cell. In proliferating tissues where cell division axes are oriented randomly, as in the fly wing (*47*), there is likely to be variation in the potency of a juxtacrine signal. This would need to be factored in when engineering a persistent zone of cells that are

required to respond uniformly to synthetic gene circuits. For instance, feedback circuits might be necessary to refine a precise region of persistent response following an initial signal activation in multiple cells within tissues. In fact, positive feedback is common to many signaling pathways and occurs during native Notch activation, for example, to form the boundary between dorsal and ventral cell populations that will form the margin of the fly wing after pupation (*48*).

Our results imply that the overall clone shape is likely to be especially important in determining the total synthetic signal output in proliferating tissues, an important consequence of the signal output being proportional to the ligand cell and receptor cell contact length (*17*). As such points of geometric inflection in the clone can substantially change the extent of cell-cell contact and in turn the strength of the synNotch output. Our results show that the clone becomes highly irregular with time and that clone morphology depends on the tension of the cell bonds at the interface (*41*). This has important implications on future strategies for building synthetic circuits and will need to be factored into strategies to shape a proliferating tissue to achieve desired synNotch outputs. In cases where the synNotch response affects proliferation, more sophisticated mathematical models will be required that can accurately predict the delicate interplay between input and output due to tissue growth and consequent cell rearrangements (*49–52*). Overall, our multi-scale approach, linking the intracellular biochemical processes of GFP synthesis and degradation, together with cell and tissue level processes such as growth and division provides a quantitative assay to study the influence of cell mechanical properties on signal patterning.

Materials and Methods

1. *Drosophila* Method Details

Drosophila Transgenes

Fly stocks were maintained at 25°C on standard corn food, and all experiments were performed at 25°C on standard corn food. All ligand and receptor coding sequences, with the exception of FSH , were inserted into a modified form of $pUAST$-$attB$ (www.flyc31.org) that contains a single Flp Recombinase Target (FRT, ' $>$ ') positioned between the UAS promoter and the coding sequence, and the resulting $UAS > FSH - Delta$ and $UAS > FSHR - synNotch$ transgenes were inserted at a single genomic docking site, $attP - 86Fb$ located on the right arm of the third chromosome and were oriented so that the promoter is centromere proximal to the coding sequence6. A single $UAS.FSH\alpha$, transgene inserted by conventional P-element mediated transformation onto the X chromosome was used in all experiments. The FSH chimeric form of Delta is described in detail in (*28*) . Briefly, the native extracellular domain of Delta was replaced in its entirety by the β subunit of human Follicle Stimulation Hormone (FSHβ) (*53*) and an HRP tag was inserted immediately downstream of the C-terminal YCSFGEMKE sequence of FSHβ and immediately upstream of the Dl transmembrane domain. In all experiments, FSHα was co-expressed with the FSHβ-Dl protein to reconstitute FSH, which is an FSHα/FSHβ heterodimer (for simplicity, we refer to the ligand as the FSH-Delta chimera and do not include the HRP tag in its designations). The FSHR-synNotch form of Notch is based on the FSHR-A2-Notch receptor described in detail6. Briefly the amino-terminal Epidermal Growth Factor (EGF) Repeat containing portion of the native extracellular domain of N was replaced by the ectodomain of FSHR. The extracellular domain was tagged by the insertion of mCherry just upstream of the juxtamembrane A2 domain. The NRR of

Notch was replaced with the force sensitive region of von Willibrand Factor A2 domain. Previous work has shown that this domain acts as a force sensor in the same way as the NRR6. The additional change to FSHR-A2-Notch to form FSHR-synNotch replaced the cytosolic domain of FSHR-A2-Notch with the LexA-VP16 trascription factor (*54*) . The join between Notch and Lex A is as follows (the Notch sequence is in uppercase): VIT-GIILVIIALAFFGMVLSTQRKRsgppkaltarqqevfdlir. Complete DNA sequences for both the ligand and receptor are available on request.

Analysis of signaling between FSH-Delta and FSHR-synNotch expressing cells

Signaling between FSH-Delta and FSHR-Notch cells was established using Mosaic Analysis by Promoter Swap (MAPS; see (*28*) for detailed description). In brief, mitotic recombination across the FRTs in cells transheterozygous for UAS>transgenes is induced in the presence of a *nub.Gal4* driver that acts in the developing wing. Upon the appropriate segregation of the recombined chromatid arms at the 4 strand stage, populations of FSH-Delta and FSHR-synNotch expressing cells were generated; the FSH-Delta expressing cells are marked by staining for the HRP epitope tag (blue in all of the Figures), and the dedicated FSHR-synNotch expressing cells are marked "black" by the absence of HRP expression. Receptor activation occurs at the interface between the cells that express FSH-Delta and those that express solely the receptor6. Here this was monitored by assaying for a GFP output, since FSHR-synNotch activation results in the translocation of the LexA-VP16 transcription factor to the nucleus and expression of a transgene composed of the LexO promoter followed by a fusion of the surface protein CD8 followed by GFP (LexO-CD8::GFP, Bloomington Stock Center). To induce mosaics by promoter swap, first or second instar larvae of the appropriate genotype

$(hsp70.flpUAS.FSH\alpha/hsp70.flporY; nub.Gal4/LexO-CD8::GFP; UAS>FSH-Delta/UAS>FSHR-synNotch)$ were heat shocked at 33°C for 20 minutes and wing discs from mature third instar larvae were dissected, fixed, stained for HRP expression and mounted for confocal microscopy [commercially available Rabbit anti-HRP (Abcam ab34885, 1/1000) antisera were used in combination with Alexa 633 conjugated labelled secondary antisera following standard protocols, e.g., as in (*28*)]. The native fluorescence of the GFP was also visualized in these preparations.

2. Vertex based modeling framework for synNotch induced gene expression

We use the vertex model to represent the *Drosophila* wing disc epithelium as a two dimensional cell layer. Using a cell-based computational framework, Virtual Leaf, we simulate coupled vertex and in addition to the chemical dynamics we implemented (*55, 56*). The two-dimensional description is a good approximation for the wing disc epithelium if changes in cell height are assumed to be negligible, Fig. 1(D). Cells in this epithelial monolayer are represented as a network of interconnected polygons (edges as straight lines connecting vertices). The configuration of each individual cell, and thus of the whole network, is characterized by the positions of the vertices, and the connections between them. Assuming cell shape relaxations occur at timescales much faster than the cell division, the stable network configuration is determined by the minima of the energy function,

$$\mathcal{E} = \sum_{\alpha} (K_A(A_\alpha - A_0)^2 + K_P(P_\alpha - P_0)^2) \tag{3}$$

where, A_α and P_α are the area and perimeter of cell α, respectively. A_0 and P_0 are the preferred area and perimeter of cell α. The summation is over all cells $\alpha = 1 \cdots N(t)$, where $N(t)$ is the total number of cells at time t. The first term describes the cell area

elasticity with an elastic coefficient K_A which results from cell volume incompressibility and the cell monolayer's resistance to height fluctuations. The second term describes the stiffness of the cell perimeter P_α with an elastic constant, K_P, and it results from two processes: contractility of the actomyosin subcellular cortex and effective cell membrane tension due to cell-cell adhesion and cortical line tension. The energy function described by Eq. (3) is widely used to study tissue mechanics during morphogenesis (*57, 58*).
A detailed description of the VirtualLeaf vertex modeling framework, which we have adapted here, is given in Ref. (*55*). The shape of a cell, and thus the whole tissue, is determined by the force balanced state, i.e., the state in which the forces, described in the energy function $\mathcal{E}$ given by Eq.(3), acting on each node have sufficiently balanced out. The simulation of this vertex model employs Monte Carlo based 'Metropolis dynamics' method to alter the positions of the vertices until the energy function, given by Eq.(3), is minimized such that all interfacial tensions are balanced by cellular pressures (*55*). We assume the mechanical properties of all the cells of both the cell types in the tissue, i.e., ligand and receptor-expressing synNotch cells, to be homogeneous and constant. The values of the model parameters are listed in the Table (1).

3. Rules governing cell growth and division

Each cell in the *in silico* tissue is fixed to the same base area, A_b. Our initial condition is such that all the cells are set to $A_\alpha = A_b = 50$, where α is the cell index. At $t = 0$, the preferred area A_0 of all the cells is equal to the base area. The dimensionless value of 50 for the cell area in the model corresponds to an experimental value of $10\mu\text{m}^2$. To implement cell area growth over time, as described in (*55*), the cell preferred area is increased in the next time step $t + \delta t$ as,

$$A_0(t + dt) = A_0(t) + g_0 dt \tag{4}$$

where, g_0 is the value by which the cells preferred area is incremented in the next time step. The cell area at each time step is relaxed quasi-statically to the preferred area, which results in an irreversible increase in the cell area over time. Over time, when the area of a cell A_α is double the base area A_b then the cell divides over its short axis, Fig. 1(D-iv). Right after division, the preferred area of the divided cell is reset to $A_0 = A_b = 50$. As a result the area of each daughter cell, the instant after cell division, is relaxed to $A_0 = A_b$.

Since the cell divides when its area A_α reaches a value which is twice the base area of the cell A_b, which occurs in the time duration τ,

$$\frac{A_0}{\tau} = g_0, \tag{5}$$

in our simulations we chose a timescale such that 1 relaxation step that minimizes the energy function E, given by Eq. (3), for the preferred $A_0(t)$ at the time t, corresponds to 1 h. We set $A(t) = A_0$, where $A_0 = 10\mu m^2$ is the typical base area of a cell in the wing disc epithelium. The typical time τ over which a wing disc epithelium cell divides is equal to 10 h. Hence, $g_0 = 1\mu m^2/h$ is the typical cell area growth rate. By dividing and multiplying both sides of Eq.(5) by a unit area $A^* = 0.2\mu m^2$ and a unit time $t^* = 1h$, respectively, we obtain,

$$\frac{\tilde{A}_0}{\tilde{\tau}} = \tilde{g}_0 \tag{6}$$

We chose the cell base area as $\tilde{A}_0 = 50$, which corresponds to the experimental value of $10\mu m^2$, and cell division time $\tilde{\tau} = 10$, which is equivalent to 10h, implying that $\tilde{g}_0 = 5$.

4. Dynamics of GFP signal pattern in synNotch cells

To characterize the spatiotemporal pattern of synNotch induced GFP output in the *Drosophila* wing disc, in addition to the dynamics of cell shape and cell division, we

incorporate a dynamic equation for the change in the number of GFP molecules in a synNotch cell. The cell GFP signal intensity at any time t in our model is proportional to the total number of GFP molecules in the cell at that time. Our modeling framework thus gives rise to a coupling between three timescales at the scale of a single cell, namely, the intracellular GFP synthesis rate, the rate of intracellular GFP degradation and the rate of cell division.

In our model, the wing disc epithelium consists of two types of cells, namely, synthetic ligand expressing cells and synthetic Notch receptor expressing cells (which we refer to as synNotch cells). The ligand expressing cells are assigned a label or cell type of 0 and the synNotch receptor cells are assigned a label or cell type of 1. This binary-type quantity T is a function of cell α, where α is the cell index, $i \in 1 \ldots N$. T takes the value $T(\alpha) = 0$ if the cell α is a ligand expressing cell and $T(\alpha) = 1$ for a synNotch receptor cell, Fig. 1(A). The total number of cells at any given time point is $N(t) = N_{(T=0)} + N_{(T=1)}$, where $N_{(T=0(1))}$ is the total number of cells of type $T = 0(1)$. We assume that the whole wing disc is fully characterized as comprising of type 0 and type 1 cells. The cell identity, $T(\alpha) = 0$ or 1, assigned to a cell is conserved across cell division events. Therefore, when a cell α of type $T(\alpha) = 0$, i.e., a ligand expressing cell, divides, it produces two daughter cells, both of which are of cell type 0. Similarly, when a cell of cell type $T(\alpha) = 1$, i.e., a synNotch cell, divides, it produces two daughter cells, both of which are cells of cell type 1. We propose that the dynamics of GFP output (G_α) as a function of t is given by,

$$\frac{dG_\alpha(t)}{dt} = S \sum_\beta \frac{l_{\alpha\beta}(t)(1 - \delta_{T(\alpha),T(\beta)})}{P_\alpha(t)} - DG_\alpha(t). \tag{7}$$

The first term on the right hand side of Eq.(7) describes GFP synthesis at the rate $S(h^{-1})$ in synNotch cells. The summation is over all cells β neighboring a cell α. GFP is

synthesized only in those synNotch receptor cells that are adjacent to the synthetic ligand expressing cells, i.e., synNotch receptor cells which share an edge or a cell bond with the ligand expressing cells. This condition is ensured in the model by the kronecker delta function $\delta_{T(\alpha),T(\beta)}$, which assumes the value 0 if the Notch cell α and its adjacent cell β are of different types, i.e., $(T(\alpha) \neq T(\beta))$, and, the value 1 if they are of the same type, i.e., $(T(\alpha) = T(\beta))$. With this condition, GFP synthesis is restricted to only those cells that share a cell-cell junction with synthetic ligand expressing cells. We propose that GFP output in a synNotch cell is proportional to the length of the cell bond, $l_{\alpha\beta}$ (μm) shared with its adjacent synthetic ligand expressing cell, and normalized to the overall perimeter P_α (μm) of the synNotch cell α at time t. The second term on the right hand of Eq.(7) accounts for the degradation of GFP in the synNotch cell α at a constant rate of D (h^{-1}).

Now, we briefly describe the non-dimensionalization of Eq.(7). By multiplying both sides of the Eq.(1) by $t^* = 1h$ we can write the dimensionless form of Eq.(1) as,

$$\frac{dG_\alpha}{d\tilde{t}} = \tilde{S} \sum_\beta \frac{\tilde{l}_{ij}(1 - \delta_{T(\alpha),T(\beta)})}{\tilde{P}_\alpha} - \tilde{D}G_\alpha \tag{8}$$

where, $\tilde{D} = Dt^*$, $\tilde{S} = St^*$, $\tilde{P} = \frac{P}{\sqrt{A^*}}$, and $\tilde{l}_{ij} = \frac{l_{ij}}{\sqrt{A^*}}$.

5. Analytical derivation showing dependence of the total synNotch GFP expression on the shape of the synNotch cell colony

The time dependent dynamics of the total GFP expression in the whole synNotch cell colony is described by the following equation,

$$\frac{dG(t)}{dt} = S \sum_{\alpha=1}^{N(t)} \sum_\beta \frac{l_{\alpha\beta}(t)(1 - \delta_{T(\alpha),T(\beta)})}{P_\alpha(t)} - DG(t) \quad . \tag{9}$$

If we assume each individual cell within the synNotch cell colony has roughly the same perimeter which is $P_\alpha = \bar{P}$ then,

$$\frac{dG(t)}{dt} \sim \frac{S}{\bar{P}} \sum_{\alpha=1}^{N(t)} \sum_{\beta} l_{\alpha\beta}(t)(1 - \delta_{T(\alpha),T(\beta)}) - DG(t) \qquad . \tag{10}$$

Let us introduce an average cell shape factor $\bar{f} = \frac{\bar{P}}{\sqrt{\bar{A}}}$, where $\bar{A}$ is the average single cell area and is defined as $\bar{A} = A_m/N_m$, with A_m being the total area of the whole synNotch cell colony, and N_m being the total number of synNotch cells in that colony in the time interval $t \in [\tau_m, \tau_{m+1}]$ between two succesive cell division events.

$$\frac{dG(t)}{dt} \sim \frac{S\sqrt{N_m}}{\bar{f}\sqrt{A_m}} \sum_{\alpha=1}^{N(t)} \sum_{\beta} l_{\alpha\beta}(t)(1 - \delta_{T(\alpha),T(\beta)}) - DG(t) \qquad . \tag{11}$$

The double summation in Eq. (11) actually results in the perimeter of the whole synNotch cell colony in the time interval $t \in [\tau_m, \tau_{m+1}]$, which we will denote by P_m.

$$\frac{dG(t)}{dt} \sim \frac{S\sqrt{N_m}}{\bar{f}\sqrt{A_m}} P_m - DG(t) \qquad . \tag{12}$$

The factor $\frac{P_m}{\sqrt{A_m}}$ in Eq. (12)is the shape factor of the whole synNotch cell colony at time t which we will denote F_m.

$$\frac{dG(t)}{dt} \sim \frac{SF_m}{\bar{f}} \sqrt{N_m} - DG(t) \qquad . \tag{13}$$

The above equation can also be written in terms of circularity of the whole synNotch clone. The circularity parameter is related to the shape factor in the following manner, $F_m = 2\sqrt{\frac{\pi}{C}}$,

$$\frac{dG(t)}{dt} \sim \frac{2S}{\bar{f}} \sqrt{\frac{\pi N_m}{C_m}} - DG(t) \qquad . \tag{14}$$

Therefore, we predict that when the circularity of the synNotch clone is small (at lower values of C_m), we expect the source term contribution to be effectively larger. This would lead to an enhanced synNotch output.

Parameter values

Table 1: Model parameters, their meaning, dimensionless values and equivalent magnitude in experimental units

Model parameter	Description	Values (Dimensionless)	Experimental values
A_b	Cell base area	50	$\sim 10\mu\text{m}^2$ (*59*)
A_0	Range of cell preferred area	[50-100]	$[10-20]\mu m^2$
P_0	Cell preferred perimeter	25	~ 11 μm (*59*)
K_A	Area elastic constant	500	
K_P	Perimeter elastic constant	100	
g_0	Cell area growth rate	5	1 $\mu\text{m}^2/h$
S	Rate of cellular GFP output	2	0.5 h^{-1}
D	Rate of cellular GFP degradation	[0-0.5]	$\sim$[0-0.5] h^{-1} (*37, 60*)
dt	Time step	1	1 h

Acknowledgments

A.M.K acknowledges funding from startup grants. P.L. acknowledges support from NICHD (R21HD107414). P.L. thanks Gary Struhl for assistance with transgene design. We thank Sumit Sinha, Xin Li, Jessica Hoffmann and Breana Walton for their valuable comments on the manuscript.

References

1. W. C. Ruder, T. Lu, J. J. Collins, *Science* **333**, 1248 (2011).

2. M. Santorelli, C. Lam, L. Morsut, *Current opinion in biotechnology* **59**, 130 (2019).

3. A. P. Liu, *et al.*, *Nature materials* **21**, 390 (2022).

4. J. A. Davies, E. Cachat, *Biochemical Society Transactions* **44** (2016).

5. J. Davies, *Development (Cambridge)* **144** (2017).

6. S. Toda, *et al.*, *Science* **370** (2020).

7. L. A. Tiemeijer, S. Sanlidag, C. V. Bouten, C. M. Sahlgren, *Trends in Biotechnology* (2022).

8. M. A. Muskavitch, *Developmental biology* **166**, 415 (1994).

9. F. Huizar, D. Soundarrajan, R. Paravitorghabeh, J. Zartman, *Developmental Dynamics* **249**, 328 (2020).

10. P. K. Grant, *et al.*, *Nature Communications* **11** (2020).

11. F. Bocci, J. N. Onuchic, M. K. Jolly, *Frontiers in Physiology* **11** (2020).

12. M. F. Simsek, E. M. Ozbudak, *Open Biology* **12** (2022).

13. A. M. Turing, *Philosophical Transactions of the Royal Society of London. Series B, Biological Sciences* **237**, 37 (1952).

14. O. Wartlick, *et al.*, *Science* **331** (2011).

15. P. Formosa-Jordan, M. Ibães, *Journal of Statistical Mechanics: Theory and Experiment* **2009** (2009).

16. U. Binshtok, D. Sprinzak, *Modeling the notch response*, vol. 1066 (2018).

17. O. Shaya, *et al.*, *Developmental Cell* **40** (2017).

18. I. Barbier, R. Perez-Carrasco, Y. Schaerli, *Molecular Systems Biology* **16** (2020).

19. E. Gazave, *et al.*, *BMC Evolutionary Biology* **9** (2009).

20. B. Zhou, *et al.*, *Signal Transduction and Targeted Therapy* **7** (2022).

21. P. D. Langridge, A. G. Diaz, J. Y. Chan, I. Greenwald, G. Struhl, *Current Biology* **32**, 2263 (2022).

22. P. A. Lawrence, G. Struhl, *Cell* **85** (1996).

23. K. W. Rogers, A. F. Schier, *Annual Review of Cell and Developmental Biology* **27** (2011).

24. M. Zecca, G. Struhl, *PLoS Biology* **19** (2021).

25. A. D. V. Rodríguez, D. Didiano, C. Desplan, *Nature Methods* **9** (2012).

26. G. Morata, P. Lawrence, *Developmental Biology* **484** (2022).

27. P. J. Bryant, P. Simpson, *The Quarterly review of biology* **59** (1984).

28. P. D. Langridge, G. Struhl, *Cell* **171** (2017).

29. C. J. Miller, L. A. Davidson, *Nature Reviews Genetics* **14**, 733 (2013).

30. E. Heller, E. Fuchs, *Journal of Cell Biology* **211**, 219 (2015).

31. T. Lecuit, L. Le Goff, *Nature* **450**, 189 (2007).

32. Y. Mao, *et al.*, *The EMBO journal* **32**, 2790 (2013).

33. A. G. Fletcher, M. Osterfield, R. E. Baker, S. Y. Shvartsman, *Biophysical Journal* **106**, 2291 (2014).

34. M. Gruening, *et al.*, *Applied Sciences (Switzerland)* **11** (2021).

35. L. Wolpert, *Journal of Theoretical Biology* **25**, 1 (1969).

36. T. Gregor, E. F. Wieschaus, A. P. McGregor, W. Bialek, D. W. Tank, *Cell* **130** (2007).

37. M. Halter, A. Tona, K. Bhadriraju, A. L. Plant, J. T. Elliott, *Cytometry Part A* **71** (2007).

38. L. He, R. Binari, J. Huang, J. Falo-Sanjuan, N. Perrimon, *Elife* **8** (2019).

39. K. E. Cavanaugh, M. F. Staddon, S. Banerjee, M. L. Gardel, *Current opinion in genetics & development* **63**, 86 (2020).

40. R. J. Huebner, *et al.*, *Elife* **10**, e65390 (2021).

41. M. Aliee, *et al.*, *Current Biology* **22**, 967 (2012).

42. D. Umetsu, *Fly* **16**, 233 (2022).

43. H. L. Stickney, M. J. Barresi, S. H. Devoto, *Developmental Dynamics* **219** (2000).

44. G. L. Hunter, *et al.*, *BMC Biology* **17** (2019).

45. M. Bischoff, *et al.*, *Nature Cell Biology* **15** (2013).

46. C. Zhang, S. Scholpp, *Current Opinion in Genetics and Development* **57**, 25 (2019).

47. M. Milán, S. Campuzano, A. García-Bellido, *Proceedings of the National Academy of Sciences of the United States of America* **93** (1996).

48. C. A. Micchelli, S. S. Blair, *Nature* **401** (1999).

49. A. N. Malmi-Kakkada, X. Li, H. S. Samanta, S. Sinha, D. Thirumalai, *Physical Review X* **8**, 021025 (2018).

50. S. Sinha, A. N. Malmi-Kakkada, X. Li, H. S. Samanta, D. Thirumalai, *Soft Matter* **16**, 5294 (2020).

51. S. Sinha, A. N. Malmi-Kakkada, *J. Phys. Chem. B* **125**, 10445 (2021).

52. A. N. Malmi-Kakkada, S. Sinha, X. Li, D. Thirumalai, *Biophysical Journal* **121**, 1 (2022).

53. Q. R. Fan, W. A. Hendrickson, *Nature* **433** (2005).

54. S. Kidd, T. Lieber, M. W. Young, *Genes and Development* **12** (1998).

55. R. M. Merks, M. Guravage, D. Inzé, G. T. Beemster, *Plant Physiology* **155** (2011).

56. I. Kneuper, *et al.*, *Journal of Experimental Botany* (2020).

57. G. Erdemci-Tandogan, M. L. Manning, *PLoS Computational Biology* **17** (2021).

58. X. Wang, *et al.*, *Proceedings of the National Academy of Sciences of the United States of America* **117** (2020).

59. M. Romanova-Michaelides, *et al.*, *Nature* **602** (2022).

60. L. He, R. Binari, J. Huang, J. Falo-Sanjuan, N. Perrimon, *eLife* **8** (2019).